CARDIFF UNIVERSITY
PRIFYSGOL CAERDYDD

ORCA – Online Research @ Cardiff

This is an Open Access document downloaded from ORCA, Cardiff University's institutional repository:https://orca.cardiff.ac.uk/id/eprint/131002/

This is the author's version of a work that was submitted to / accepted for publication.

Citation for final published version:

Mikhaylov, Roman, Wu, Fangda, Wang, Hanlin, Clayton, Aled , Sun, Chao, Xie, Zhihua , Liang, Dongfang, Dong, Yinhua, Yuan, Fan, Moschou, Despina, Wu, Zhenlin, Shen, Minghong, Yang, Jian , Fu, Yong Qing, Yang, Zhiyong , Burton, Christian, Errington, Rachel , Wiltshire, Marie and Yang, Xin 2020. Development and characterisation of acoustofluidic devices using detachable electrodes made from PCB. Lab on a Chip 20 (10) , pp. 1807-1814. 10.1039/C9LC01192G

Publishers page: http://dx.doi.org/10.1039/C9LC01192G

Please note:
Changes made as a result of publishing processes such as copy-editing, formatting and page numbers may not be reflected in this version. For the definitive version of this publication, please refer to the published source. You are advised to consult the publisher's version if you wish to cite this paper.

This version is being made available in accordance with publisher policies. See http://orca.cf.ac.uk/policies.html for usage policies. Copyright and moral rights for publications made available in ORCA are retained by the copyright holders.

Supplementary Information

Development and Characterisation of Acoustofluidic Devices Using Detachable Electrodes Made from PCB.

Roman Mikhaylov[1], Fangda Wu[1], Hanlin Wang[1], Aled Clayton[2], Chao Sun[3], Zhihua Xie[4], Dongfang Liang[5], Yinhua Dong[6], Fan Yuan[7], Despina Moschou[8], Zhenlin Wu[9], Ming Hong Shen[10], Jian Yang[10], Yongqing Fu[11], Zhiyong Yang[12], Christian Burton[1,2], Rachel J. Errington[2], Marie Wiltshire[2], Xin Yang[1]

[1] Department of Electrical and Electronic Engineering, School of Engineering, Cardiff University, Cardiff CF24 3AA, UK

[2] Tissue Micro-Environment Group, Division of Cancer & Genetics, School of Medicine, Cardiff University, Cardiff CF14 4XN, UK

[3] School of Life Sciences, Northwestern Polytechnical University, 710129, P.R. China

[4] Department of Civil Engineering, School of Engineering, Cardiff University, Cardiff CF24 3AA, UK

[5] Department of Engineering, University of Cambridge, Cambridge CB2 1PZ, UK

[6] Department of Neurology, Tianjin 4th Centre Hospital Affiliated to Nankai University, 300140, P.R. China

[7] Department of Biomedical Engineering, School of Engineering, Duke University, NC 27708-0281, USA

[8] Centre for Biosensors, Bioelectronics and Biodevices (C3Bio) and Department of Electronic & Electrical Engineering, University of Bath, Bath BA2 7AY, UK

[9] School of Optoelectronic Engineering and Instrumentation Science, Dalian University of Technology, 116023, P.R. China

[10] Preclinical Studies of Renal Tumours Group, Division of Cancer and Genetics, School of Medicine, Cardiff University, Cardiff CF14 4XN, UK

[11] Faculty of Engineering and Environment, Northumbria University, Newcastle Upon Tyne, Newcastle NE1 8ST, UK

[12] School of Mechanical Engineering, Tianjin University, 300072, P.R. China

S1. Mechanical characterisation of the IDE on PCB

The dimensions of the interdigital electrodes (IDEs) shown in Fig. 2a were measured using a calibrated reflected light microscope (KERN, Germany) with a 10× objective lens. The IDE width and spacing were found to be 38.7±3.1 µm (average ± SD) and 61.1±3.0 µm (average ± SD), respectively (Fig. S1, n = 161), resulting in a wavelength of 199.6±4.8 µm (average ± SD).

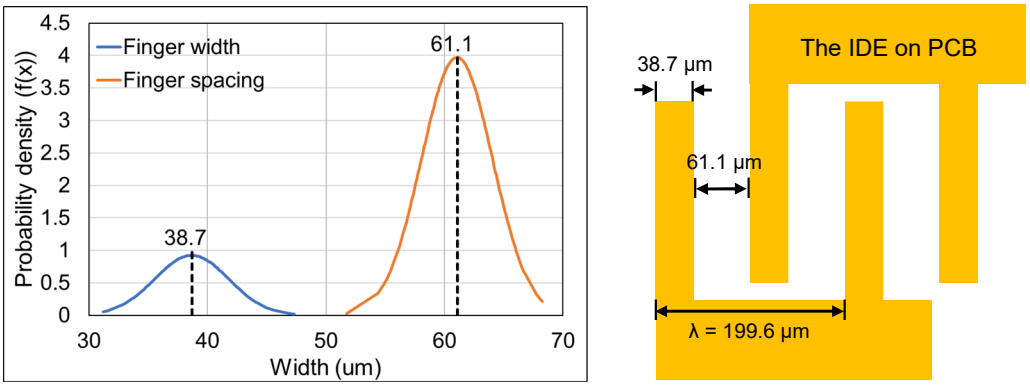

Supplementary Figure 1. The average width and spacing of finger electrodes on the PCB are 38.7 and 61.1, respectively (n = 161).

S2. Electrical characterisation

The left and right IDTs form a two-port network, as shown in Fig. S2a, whose *S*-parameters can be measured by using a vector network analyzer (VNA, E5061B ENA, Keysight) to indicate the contact between the PCB IDE and the $LiNbO_3$ wafer. The VNA measurements include: S_{11} – power reflection coefficient seen at the left IDT (Port 1), S_{21} - power transmission coefficient from the left to the right IDT (Port 1 to Port 2), S_{12} - power transmission coefficient from the right to the left IDT (Port 2 to Port 1), and S_{22} - power reflection coefficient seen at the right IDT (Port 2).

Due to the contact between the PCB IDE and the $LiNbO_3$ wafer was formed by mechanical clamping, the power reflections from both Port 1 and Port 2 are high, which could result in inefficient power transmission between the RF power amplifier and the PCB-SAW device. To counteract this, an impedance matching network (MN)[1] as shown in Fig. S2b was developed for both the left and the right IDTs to bring their impedances close to 50 Ω. Fig. S2c shows the S_{11} and S_{22} of the PCB-SAW device with and without the use of the MNs, which denotes a significant reduction on reflection from -2.7 dB to -18.4 dB and from -1.7 to -21.4 dB, respectively ('_MN' is the parameter with addition matching network in all figures). Fig. S2d shows the Smith charts

of both IDTs with and without MN, which proved that the impedances of the two IDTs were significantly improved towards 50 Ω by adding MNs. To understand the insertion loss of the PCB-SAW device, transmission coefficients, S_{12} and S_{21}, were also measured as the result shown in Fig. S2e, which also confirmed that the added MNs improve power transmission from one IDT to the opposite one.

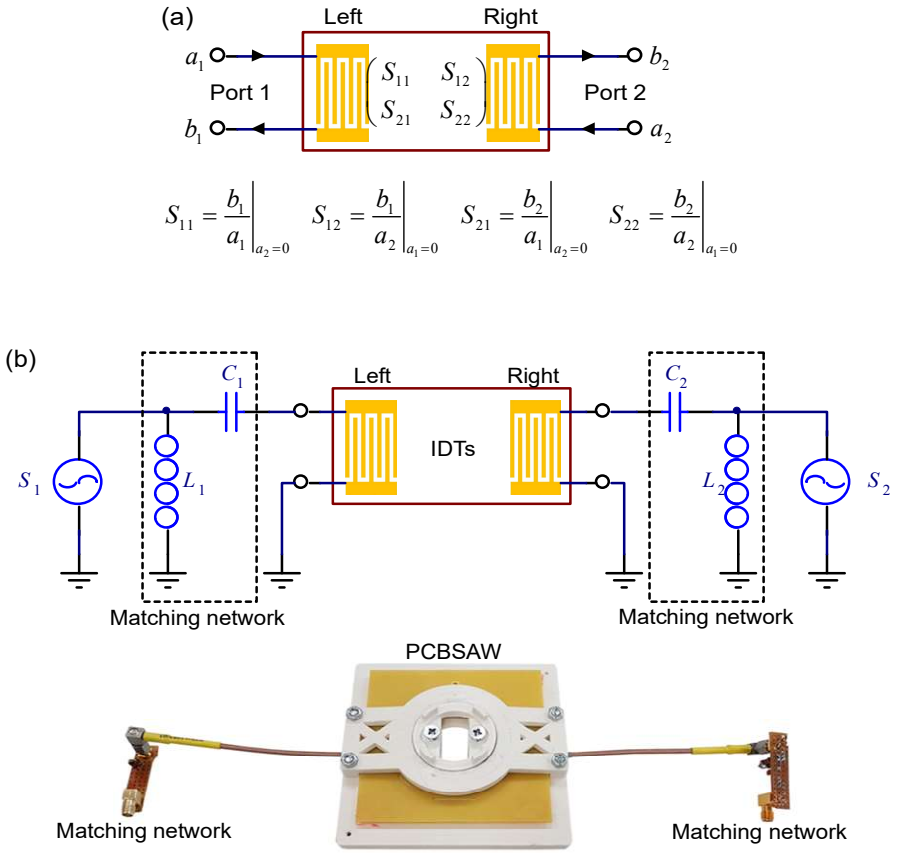

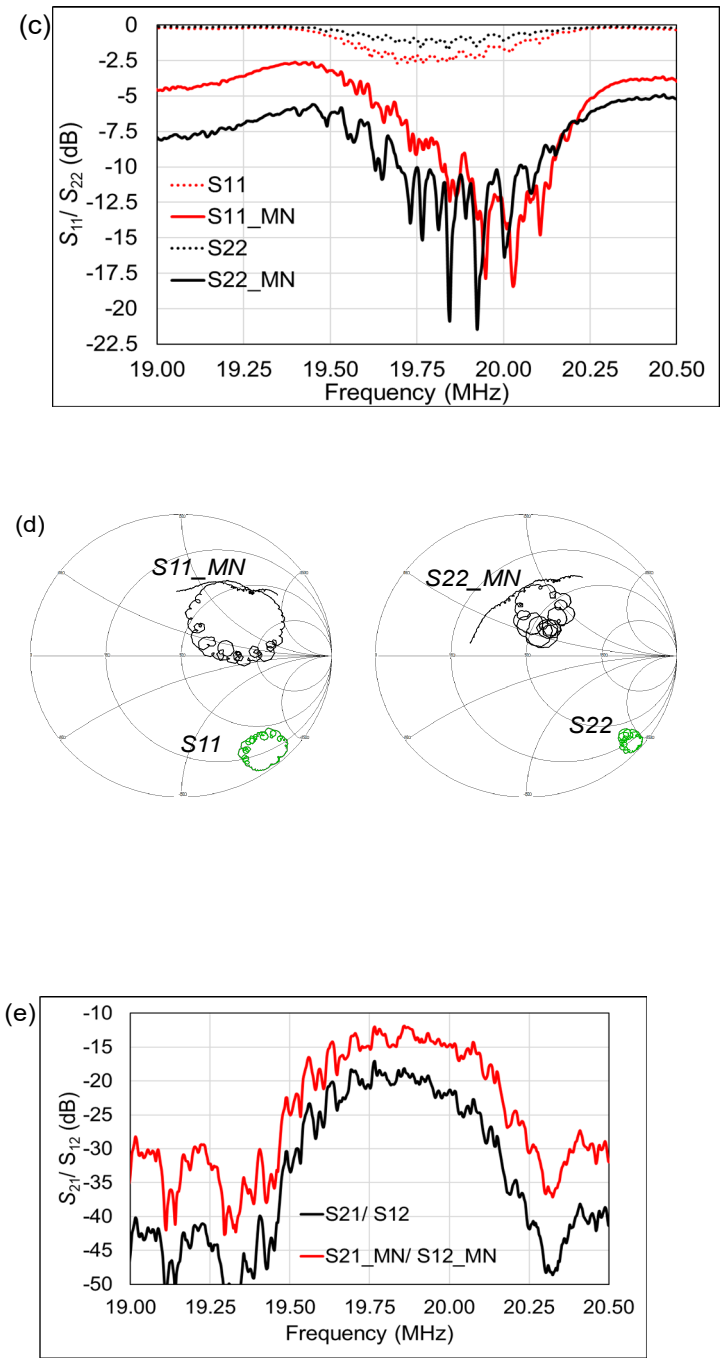

Supplementary Figure 2. Electrical characterisation to the PCB-SAW device. (a) Equivalent circuit of the two-port PCB-SAW device and the *S*-parameters. (b) Matching networks are added to couple the PCB-SAW device to RF signals. (c) Reflection coefficients of the PCB-SAW device with and without the use of matching networks. (d) Smith charts of the PCB-SAW device with and

without the use of matching networks. (e) Transmission coefficients of the PCB-SAW device with and without the use of matching networks.

To test the stability and repeatability of the PCB-SAW assembly and the readout of Rayleigh mode frequency from *S*-parameter measurements, the device was assembled and disassembled multiple times (n=23). The Rayleigh mode frequency was identified at which the S_{11}/S_{22} was minimum or S_{12}/S_{21} was maximum. As shown in Fig. S3a, in general, the addition MNs slightly increased the average Rayleigh mode frequency. For the frequency readout from S_{11} and S_{22}, the average frequencies moved from 19.77±0.08 MHz (average ± SD) to 19.82±0.13 MHz, and from 19.80±0.10 MHz to 19.89±0.11 MHz, respectively. While for S_{12} or S_{21}, the average frequency moved from 19.82±0.06 MHz (average ± SD) to 19.85±0.04 MHz. The frequency shift was because of the additional inductance and capacitance introduced by the MNs. Furthermore, the average reflection coefficients were consistently reduced from -2.7 dB to -25.2 dB, and from -2.4 dB to -27.8 dB, respectively, as shown in Fig. S3b. Similar improvement produced by the MNs also happened to the transmission coefficients as the measurement results shown in Fig. S3c, from -18.1 dB to -12.1 dB. The assembly and disassembly tests confirmed that the change to the Rayleigh mode frequency of the PCB-SAW device was within a small range, which allowed a stable SAW wavelength to produce for applications. The use of MNs improved the electrical characteristics of the PCB-SAW device.

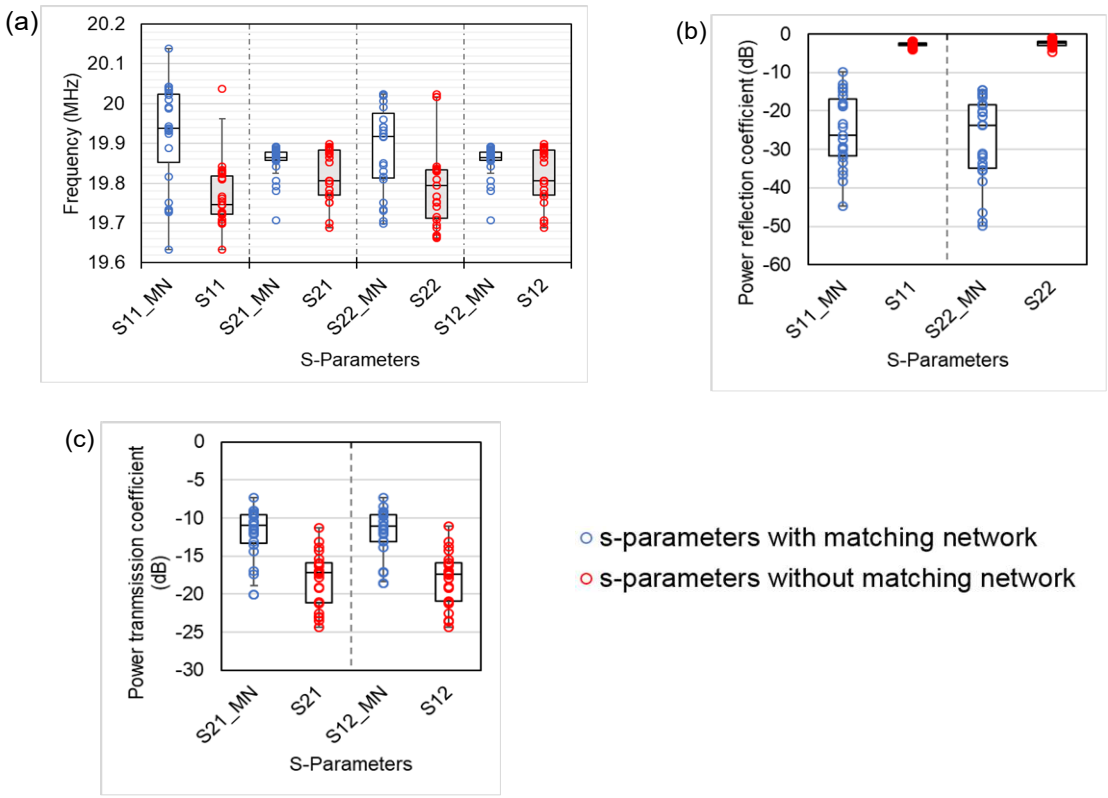

Supplementary Figure 3. *S*-parameter characterisation of the PCB-SAW device. (a) The readout of Rayleigh mode frequencies from S_{11}, S_{22}, S_{21} and S_{12} measurements with and without the MNs. (b) The reflection coefficients of the PCB-SAW device with and without the MNs. (c) The transmission coefficients of the PCB-SAW device with and without the MNs.

To find out which working frequency identified from the readout of *S*-parameters produced the optimal power transmission, the device was then configured in the measurement as the setup shown in Fig. S4a, in which a coupler was used to couple the RF signal to the PCB-SAW device while interfacing with two power meters (PM_1 and PM_2) to monitor the incident and reflected powers of one IDT. The difference between the incident and reflected powers was the input power of the device. A third power meter (PM_3) was connected to the opposite IDT to measure the transmitted power. By using four different working frequencies determined by the readout of the four *S*-parameters, the transmitted powers were recorded as shown in Fig. S4b and S4c. Generally, the addition MNs improved the power transmission in all cases, and the working frequency determined by the readout of S_{21} or S_{12} showed the largest power transmission.

To prove that the optimal working frequency determined by the readout of S_{21} or S_{12} was reliable, the input power was fixed at -10 dBm while the input frequency was tuned slightly above and below the optimal working frequency. As shown in Fig. S4d, the transmitted power recorded by the power meter informed that the maximum power transmission took place at 19.871 MHz, which was in a good agreement with the readout from S_{21} or S_{12}. The result indicated that one can use the VNA readout of S_{21} or S_{12} to predict the optimal working frequency of the PCB-SAW device.

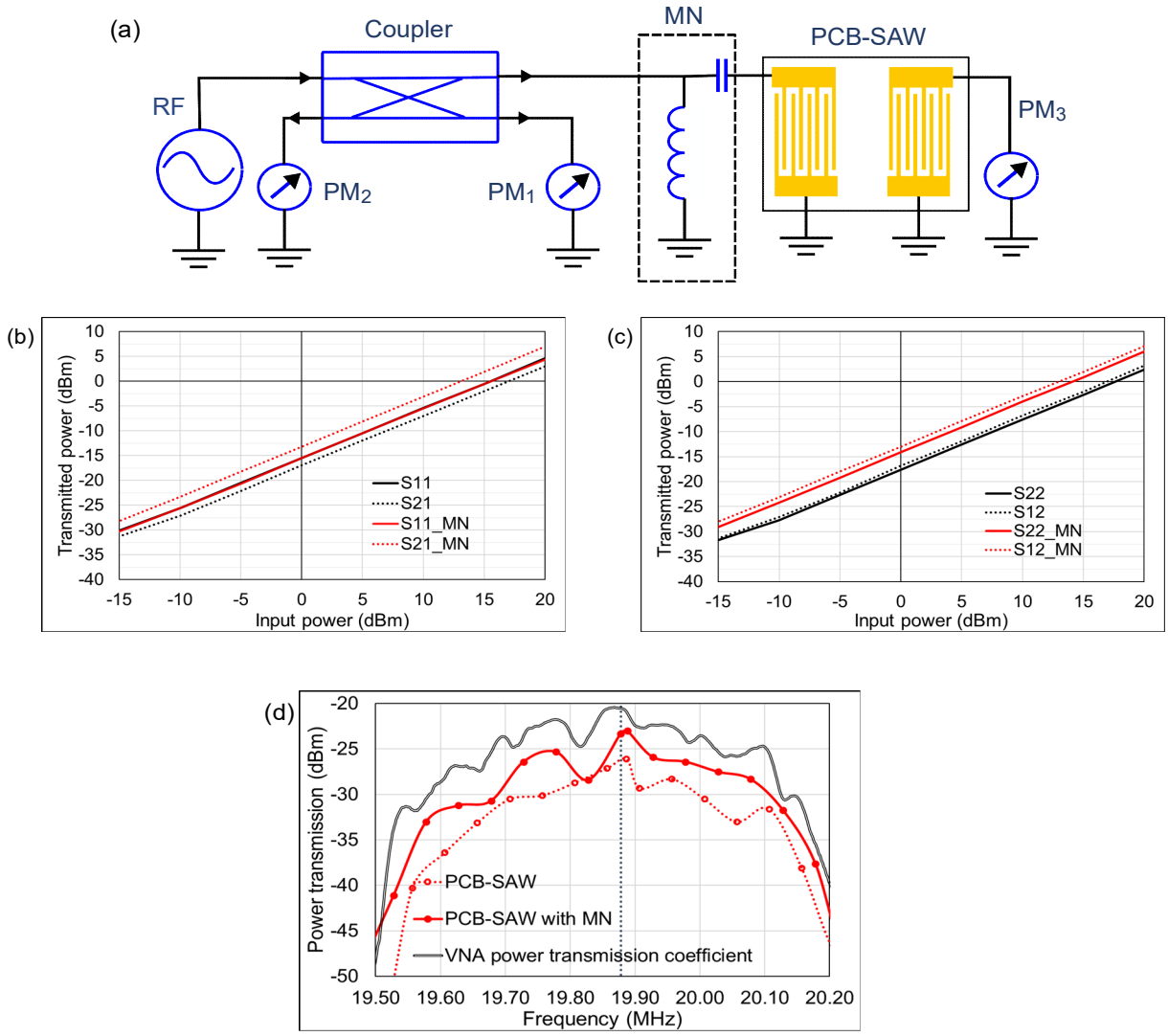

Supplementary Figure 4. Investigation of the power operation and determination of the optimal working frequency for the PCB-SAW device. (a) The measurement setup of the power transmission test. (b) and (c) The transmitted power versus input power at different working frequencies identified by readouts of four *S*-parameters. (d) The agreement on the optimal working

frequency between the power transmission measurement and the VNA readout. The vertical dotted line indicates the frequency from S_{21} readout.

S3. The PCB-SAW device modelling

To study the distribution of acoustic pressure and predict microparticle trajectories in the PCB-SAW device, COMSOL Multiphysics® was used to compute the numerical results on the X-Z plane of the microchannel. Figs. S5a and S5b show the distribution of the acoustic pressure when pressure node (PN) and pressure anti-node (AN) formed at the centre of the microchannel, respectively. Particle trajectories corresponding to both conditions are given in Figs. S5c and S5d, respectively. The first case indicates three particle aggregation traces (red dots in Fig. S5c) on the plane, two of which are close to the walls of the microchannel. The second case creates a more complex particle aggregation traces on the plane. It is worth noting that the particle aggregation at the centre (the yellow dot in Fig. S5d) is unstable due to the occurrence of force imbalance, i.e. $\sum \boldsymbol{F}_x \neq 0$, thus in reality microparticles migrated to the centre tend to be attracted towards adjacent stable PN locations (pointed by green and black arrows), resulting in low probability of trapped microparticles in the centre, which is in a good agreement with microsphere and cell experiments. In addition, two approximated aggregation traces (pointed by green or black arrows) are expected to form a combined particle trace under microscope.

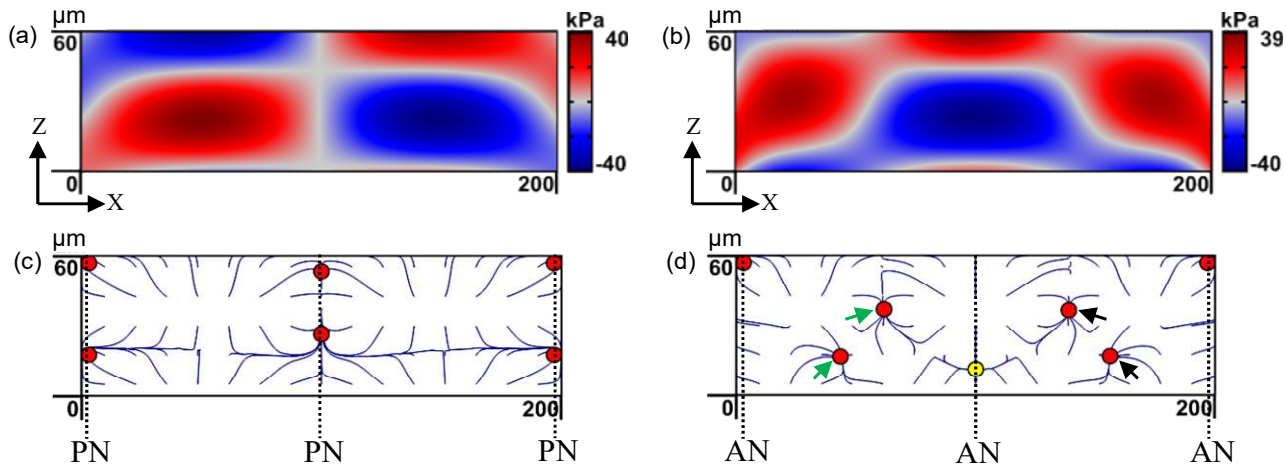

Supplementary Figure 5. COMSOL Multiphysics® simulation of the PCB-SAW device. (a) Acoustic pressure when PN located at the centre of the microchannel. (b) Acoustic pressure when

AN located at the centre of the microchannel. (c) Particle trajectories for PN located at the centre of the microchannel. (d) Particle trajectories for AN located at the centre of the microchannel.

References

1. Lackey, J. E. *Fundamentals of electricity and electronics. 579p.* (Holt Rinehart, 1983).